Journal of Molecular Catalysis A: Chemical 344 (2011) 145–152

Contents lists available at ScienceDirect

Journal of Molecular Catalysis A: Chemical

journal homepage: www.elsevier.com/locate/molcata

# Degradation of PCP-Na with La–B co-doped $TiO_2$ series synthesized by the sol–gel hydrothermal method under visible and solar light irradiation

J.W. Liu [a], R. Han [a,*], H.T. Wang [a,**], Y. Zhao [a], W.J. Lu [a], H.Y. Wu [a], T.F. Yu [b], Y.X. Zhang [a]

[a] Department of Environmental Science and Engineering, Tsinghua University, Beijing 100084, People's Republic of China
[b] School of Chemical and Environmental Engineering, China University of Mining and Technology, Beijing 100083, People's Republic of China

ARTICLE INFO

*Article history:*
Received 3 December 2010
Received in revised form 29 April 2011
Accepted 30 April 2011
Available online 8 May 2011

*Keywords:*
Photocatalysis
Hydrothermal process
Titania modification
Dopant

ABSTRACT

A series of photocatalysts was synthesized by doping $TiO_2$ with La and B via the sol–gel hydrothermal route. The photocatalytic capability of the catalysts under visible and solar light was evaluated in terms of sodium pentachlorophenate (PCP-Na) decomposition and dechlorination. The structural and physicochemical properties of these nanocatalysts were characterized by XRD, DRS, ICP-OES, TEM, XPS, and $N_2$ adsorption–desorption techniques. B doping enlarged the anatase framework, and La doping hindered the crystallization and growth of the mesoporous structure in both singly La-doped and La–B co-doped catalysts. B implantation mainly resulted in visible-light response, whereas overload $La_2O_3$ coating worsened visible light absorption, as confirmed by DRS and XPS. XPS and ICP-OES analyses revealed that the B and La content increased approximately by 1.6 and 4.8 times from the interior to the surface of modified $TiO_2$, which dominantly existed in the form of $La_2O_3$ and interstitial B structure. The co-doped sample with 1% La and 5% B doping (LA10B50) exhibited maximum photocatalytic activity under visible and solar light compared with the mono-doped samples, which was attributed to synergetic effects, namely, efficient separation of photo-generated carriers by La and response to the extended visible region due to B. An increase in hydroxyl groups and the photosensitivity of carbon on the surface also contributed to the improvement of photoactivity.



## 1. Introduction

$TiO_2$ nanoparticles have attracted attention in research on the photo-induced removal of harmful environmental contaminants due to their high photocatalytic potential [1–3]. However, two problems limit the use of $TiO_2$: its poor response to visible light (accounting for 45% of solar energy) due to its wide bandgap, and the fast recombination of the photo-generated electron–hole pairs on its surfaces or in its lattices [2]. Both the wide bandgap resulting in the selective ultraviolet (UV, $\lambda < 380$ nm) induction of the catalyst and the poor separation efficiency of the electron–hole pairs (approximately 90% of the generated carriers lost within nanoseconds of their generation) leading to low photocatalytic activity can limit the solar applications of $TiO_2$ [4].

The photocatalytic performance of $TiO_2$ can be improved by doping with impurities such as nonmetals, metal ions, and semiconductor oxides [5]. Incorporation of non-metal atoms, such as nitrogen [6,7], sulfur [8,9], carbon [3,10], and phosphorus [11], has been demonstrated to enhance visible light absorption and photocatalytic activity. B modification by the sol–gel, surface impregnation, and ion implantation methods can also result in the absorption of visible light and changes in the chemical state [12–14].

Increasing attention has been given to metal doping (i.e., the development of higher visible light-active photocatalysts by doping with transition metals) [15,16]. However, even the relatively low doping content of transition metals does not always lead to better photocatalytic activity due to the increased recombination efficiency of electron–hole pairs [5]. Lanthanide ions have also been proven to be good dopants for the activity of $TiO_2$ photocatalysts by improving the microstructure and increasing the separation efficiency of electron–hole pairs [17,18]. The fabrication of novel La–B co-doped $TiO_2$ photocatalysts by the sol–gel hydrothermal process was investigated in our study. Attention was paid not only to the variation of catalytic activity with the incorporation of the dopant but also to the action of the dopants in this co-doped system.

Highly chlorinated phenol derivatives such as sodium pentachlorophenate (PCP-Na) are typical hazardous organic pollutants, and they have been listed as priority contaminants by the US, European Union, and China [19,20]. There have been some investigations to examine their degradation by photo-Fenton reaction [20,21], enzymatic reaction [22], and photocatalysis [23].

* Corresponding author. Tel.: +86 13811484571; fax: +86 10 62773438.
** Corresponding author. Tel.: +86 10 62773438; fax: +86 10 62773438.
*E-mail addresses:* han-r07@mails.tsinghua.edu.cn (R. Han), htwang@mail.tsinghua.edu.cn (H.T. Wang).

1381-1169/$ – see front matter © 2011 Elsevier B.V. All rights reserved.
doi:10.1016/j.molcata.2011.04.022

However, PCP-Na has not been used as a model target contaminant in investigating its removal in the photocatalytic process by modified catalysts under solar light.

Previously, the photocatalytic activity of doped catalysts was examined under the irradiation of visible light and simulated sunlight sources, such as xenon lamps, which are different from real sunlight. In this study, novel La–B $TiO_2$ nanoparticles were employed to investigate the effects of photocatalytic reaction on the efficiency of PCP-Na degradation under visible ($\lambda > 400$ nm) and solar light. The degradation process was examined by ion chromatography (IC), high-performance liquid chromatography (HPLC), and UV–vis spectroscopy (UV). In this work, several important factors affecting photocatalytic activity, such as the layer feature, crystallinity, amount of the dopant, distribution of the dopant, and light absorption, were also systematically investigated.

## 2. Experimental

### 2.1. Catalyst preparation

La-doped $TiO_2$, B-doped $TiO_2$, and La–B co-doped samples were prepared by the sol–gel hydrothermal method as follows. Under vigorous stirring, 0.05 mol $Ti(OBu)_4$ was added to 0.2 mol isopropyl alcohol. A desired amount of $H_3BO_3$ and $La(NO_3)_3{\cdot}6H_2O$ was dissolved in a solution of acetic acid (15 mL), isopropyl alcohol (10 mL), and deionized water (20 mL). This mixture was added dropwise into the titanium-isopropyl alcohol solution, which was stirred for 4 h at room temperature until a transparent gel was formed.

The $TiO_2$ gel (approximately 70 mL) obtained was transferred to a Teflon vessel (100 mL) and heated at 180 °C for 12 h. The vessel was cooled to room temperature. After centrifugation at 5000 rpm for 10 min, the obtained precipitate was washed with deionized water and ethanol, dried at 80 °C for 8 h, then dried again at 180 °C for 12 h to remove organic contaminants. The samples mono-doped with La (La/Ti molar ratios of 1%, 2%, and 5%) were denoted as TLA10, TLA20, and TLA50, respectively. Samples mono-doped with B (B/Ti molar ratios of 2%, 5%, and 10%) were denoted as TB20, TB50, TB100, respectively. The non-doped titanium and La–B co-doped catalysts were named NT0, LA10B20, and LA10B50, also according to the molar ratio of the doped element. The synthesized gels of pure $TiO_2$, 1% La–$TiO_2$, 5% B–$TiO_2$, and 1% La–% B–$TiO_2$ dried at 80 °C without the hydrothermal process were denoted as NT0-80, TLA10-80, TB50-80, and LA10B50-80, respectively. The commercial P25 $TiO_2$ (80% anatase, 20% rutile; BET area, 50 $m^2\ g^{-1}$) supplied by Degussa Corporation (Germany) was used for comparison.

### 2.2. Characterization of the photocatalysts

The crystal structure of the samples was analyzed by X-ray diffraction (XRD) using a Bruker D8 Advance diffractometer with Cu $K_\alpha$ line at $\lambda = 1.5418$ Å and settings at 40 kV and 40 mA. Nitrogen adsorption–desorption isotherms were obtained at 77 K using an Autosorb AS-1 $N_2$ adsorption apparatus (Quantachrome Instruments, USA) after the samples were vacuum-degassed at 150 °C. The surface area of the modified $TiO_2$ nanoparticles was determined from the adsorption data using the Brunauer–Emmett–Teller (BET) model, and the pore volume based on the desorption isotherms was obtained using the Barrett–Joyner–Halenda (BJH) model. Transmission electron microscope (TEM) images were obtained with a Hitachi H-800 transmission electron microscope operating at an accelerating voltage of 200 kV. UV–vis diffuse reflectance spectra (DRS) were taken using a Hitachi U-3010 spectrophotometer equipped with an integrating sphere accessory for diffuse reflectance. The surface composition of the nanocatalysts was analyzed on a Kratos Axis Ultra System with monochromatic Al $K_\alpha$ X-rays (1486.6 eV). Determination of element composition in the catalysts was performed by microwave digestion and the inductively coupled plasma optical emission spectroscopy (ICP-OES) method using an IRIS Intrepid II XSP Spectrometer (ThermoFisher, USA).

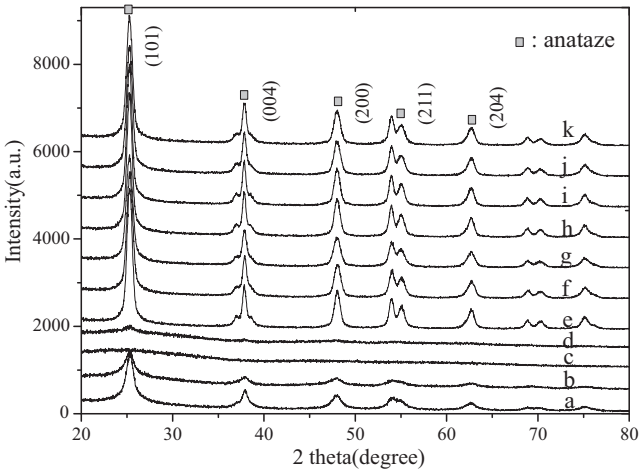


**Fig. 1.** X-ray diffraction patterns of the (a) NT0-80, (b) TB50-80, (c) TLA10-80, (d) LA10B50-80, (e) NT0, (f) TLA10, (g) TLA20, (h) TB20, (i) TB50, (j) LA10B20, and (k) LA10B50 catalysts.

### 2.3. Photocatalytic degradation

Photocatalytic degradation was performed in a glass reactor containing 500 mL 20 ppm PCP-Na solution and 200 mg of the photocatalyst. Visible light photocatalytic tests were performed using an 800 mL cylindrical reactor equipped with a quartz cool trap with 2 M $NaNO_2$, which was used as cut-off filter to remove UV radiation from the 400 W Xe lamp and water cooler to keep the reaction temperature at 20 °C. Solar light photocatalytic experiments were performed with a circular disk (diameter: 20 cm; height: 3 cm; total capacity: 940 mL) covered with a quartz slice to maintain the solar light spectrum. The solar irradiation strength was 20.6–37.9 mW/$cm^2$ as measured by a radiometer (FZ-A, Photoelectric Instrument Factory of Beijing Normal University) from 2 to 4 PM in May at Beijing.

Reactions under visible and solar light illumination were initiated after 60 min stirring in the dark. First, 8 mL of the mixture was withdrawn at predetermined intervals, and then centrifuged and filtered through a 0.45 μm pore size membrane filter to remove the catalyst particles. The determination of PCP-Na in the filtrates was performed by HPLC (Shimadzu model LC-10AVP) equipped with a YMC C-18 (25 μm × 4.6 mm × 250 mm) reverse phase column and a UV detector at 249 nm. The mobile phase was 80% methanol in phosphate buffer (pH = 2), and the flow rate was 1.0 mL/min. The variation of chloride ion evolution was monitored by an ion chromatography system (ICS-1000, Dionex Corporation). The UV spectra of the aqueous solutions were obtained on a UV-2401PC (Shimadzu). The photocatalytic capability of the modified $TiO_2$ was studied by observing the rate constant of PCP-Na degradation based on a pseudo-first-order reaction model and the dechlorination rate of PCP-Na.

## 3. Results and discussion

### 3.1. XRD patterns

The crystalline phase of the La–B–$TiO_2$ series was characterized by XRD measurements. Fig. 1 displays the XRD patterns of the

**Table 1**
Physicochemical properties of undoped and La-, B-, and La–B co-doped titanium catalysts.

| Sample | Crystalline size[a] (nm) | Intensity (1 0 1)[b] (a.u.) | Surface area[c] ($m^2$/g) | Pore volume[d] ($cm^3$/g) | Pore diameter[e] (nm) |
|---|---|---|---|---|---|
| NT0 | 12.0 | 3244 | 116.131 | 0.253 | 8.558 |
| TLA10 | 10.4 | 2781 | 126.151 | 0.245 | 7.592 |
| TLA20 | 9.7 | 2470 | 128.437 | 0.234 | 7.365 |
| TB20 | 12.1 | 3249 | 123.208 | 0.275 | 8.826 |
| TB50 | 13.3 | 3305 | 119.156 | 0.281 | 9.256 |
| LA10B20 | 10.8 | 3011 | 127.036 | 0.260 | 7.987 |
| LA10B50 | 10.5 | 2947 | 130.809 | 0.257 | 7.725 |

[a] Average crystallite size determined by XRD using the Scherrer equation.
[b] Intensity (1 0 1) is the height intensity of the (1 0 1) diffraction peak.
[c] Specific surface area data calculated from the multi-point BET method.
[d] Pore volume obtained from the nitrogen adsorption volume at $P/P_0$ of 0.993.
[e] Pore diameter estimated from the desorption isotherm by the BJH model.

prepared catalysts after the hydrothermal process at 180 °C and four samples without hydrothermal processing. The results show anatase patterns [i.e., 2$\theta$ values of 25.3°, 37.8°, 48.0°, 55.1° and 62.7° corresponding to the (1 0 1), (0 0 4), (2 0 0), (2 1 1), and (2 0 4) crystal planes, respectively (JCPDS 21-1272)] [24]. Peaks caused by impurities were not found. These results indicate that the doping of La and B by sol–gel hydrothermal reaction had no deleterious effect on the formation of the anatase crystal phase. Meanwhile, the $La_2O_3$ and $B_2O_3$ structures were not observed in any of the samples modified with boric acid and $La(NO_3)_3$.

Table 1 shows that the estimated anatase crystallite sizes from the (1 0 1) peak using the Scherrer formula were 12.0, 10.4, 9.7, 12.1, and 13.3 nm for NT0, TLA10, TLA20, TB20, and TB50, respectively. The crystallite size became smaller as the La concentration increased; the effect was slightly larger with B doping. For the co-doped LA10B50 catalyst, the estimated anatase crystallite size decreased to 10.5. The height of the main (1 0 1) diffraction peak also gave a quantitative view of the crystallization degree (Table 1). The peaks of the La-doped $TiO_2$ and La–B co-doped $TiO_2$ were observed to become less intense, indicating a lower crystallinity and a smaller crystallite size, compared with the pure $TiO_2$ and B-doped $TiO_2$ [25]. Moreover, Fig. 1 also shows that the crystallization of TLA10-80 and LA10B50-80 at a low temperature without the hydrothermal process was hindered compared with the result of NT0-80 and TB50-80. The X-ray diffraction patterns imply that doping La within the $TiO_2$ matrix hindered crystallization and agglomeration of the modified particles during the synthesis process.

### 3.2. BET surface areas and pore distributions

Nitrogen adsorption–desorption isotherms and the BJH pore size distribution curves (inset) were used to investigate the effect of the dopant on the porous structure of the synthesized catalysts (Fig. 2). The adsorption isotherms of the samples have the typical type IV shape with a hysteresis loop, indicating the existence of well-developed mesopores in their framework [17,26]. By comparing the pore size distribution, average pore diameter, and BJH pore volume of the catalysts (Table 1), the mesoporous structure was found to be enlarged when doped with B, whereas the pore size decreased when the catalyst was mono-doped with La and co-doped with La and B. These indicate that the doping of La can stabilize the small mesoporous framework. The calculated pore size distribution from the desorption branch of the nitrogen isotherm suggested that NT0, TLA10, and LA10B50 had a narrow pore size distribution with a maximum of approximately 7.8, 6.6, and 7.8 nm, respectively, compared with that of TB50. The average pore size, pore volume, and BET-specific surface areas were 9.256 nm, 0.28 $cm^3$/g, and 119.156 $m^2$/g for TB50, and 7.725 nm, 0.257 $cm^3$/g, and 130.809 $m^2$/g for LA10B50. These results show a remarkable increase in surface area with the use of La in the co-doped $TiO_2$ system. The enhancement of specific surface area occurred in every modified catalyst, especially the La–B co-doped titania.

### 3.3. UV–vis diffuse reflectance spectra

Fig. 3 shows the UV–vis diffuse reflectance spectra for the nanoparticles synthesized by the sol–gel hydrothermal process at various doping ratios. All samples had a stronger absorption in visible light than P25 $TiO_2$ due to the doped elements and the additional contaminated surface carbohydrate [10]. The absorption band of TLA10 presented a slight shift to the infrared region. However, increasing the La doping to 5 at.%, the spectrum of TLA50 presented a worse absorption tail in the visible region between 400 and 500 nm. The latter may be due to the increased concentration of the white $La_2O_3$ depositing on the surface of $TiO_2$ as analysis in XPS and ICP [27]. The absorption spectra of TB20 and TB50 showed that an increase in B doping led to a red shift, which can be ascribed to the formation of an impurity energy level within the bandgap [28]. The band energy $E_g$ can be calculated from the Kubelka–Munk equation, which is shown in Fig. 3 (inset). The corresponding bandgaps for NT0, TLA10, TLA50, TB20, TB50, and LA10B50 were 2.89, 2.78, 2.85, 2.66, 2.54, and 2.57 eV, respectively. Compared with the $E_g$ of TLA10 and TB50, that of LA10B50 was much higher than that of TLA10, but slightly lower than that of TB50. These results demonstrate that the visible light absorption of the co-doped catalysts dominantly resulted from B doping.

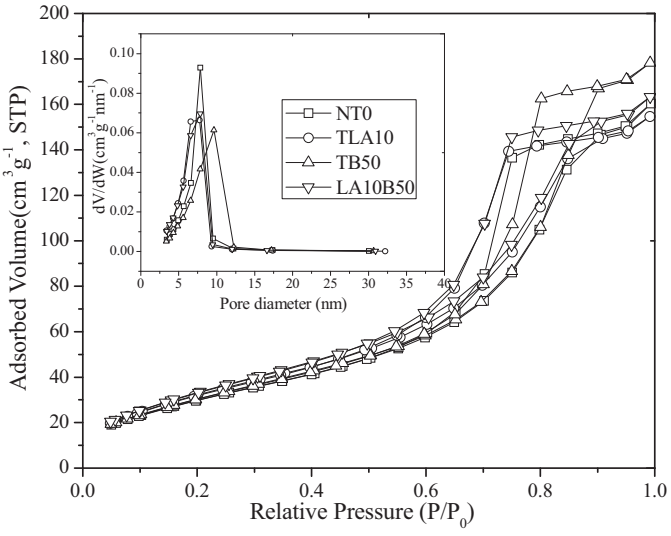


**Fig. 2.** Nitrogen adsorption–desorption isotherms and pore size distribution curves (inset) of modified $TiO_2$.

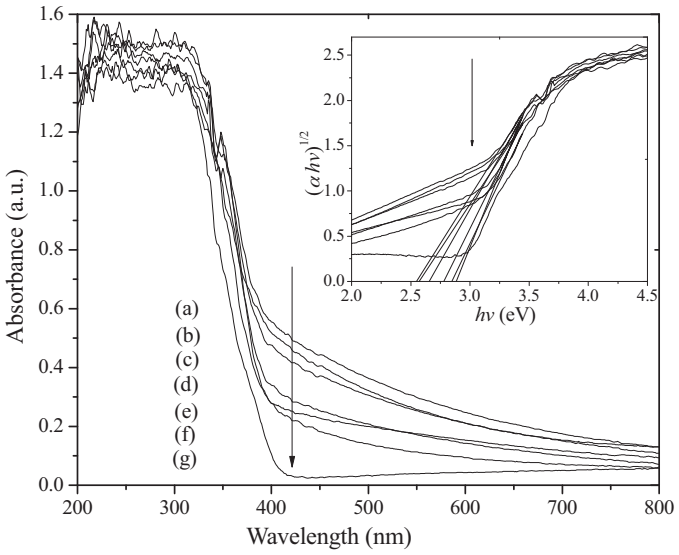


**Fig. 3.** The UV–vis diffuse reflectance spectra and the corresponding band energy (inset) of (a) TB50, (b) LA10B50, (c) TB20, (d) TLA10, (e) TLA50, (f) NT0, and (g) P25 $TiO_2$ catalysts.

### 3.4. TEM images

Fig. 4 shows the TEM photographs of NT0, TLA10, TB50, and LA10B50. From the images, all samples are elliptical particles with diameters in the range of 10–18 nm. TLA10 and LA10B50 modified with La exhibited a more anomalous morphology than NT0 and TB50 without La doping. In addition, the particle sizes of the LA10B50 and TLA10 catalysts were smaller than those of the TB50 and NT0 in general, which can be attributed to the $La_2O_3$ deposits on the surface of the catalysts [29]. The smaller particle size and the $La_2O_3$ coating may enhance the photocatalytic activities by increasing the active reaction sites and by efficiently separating charge carriers [26,27,30].

### 3.5. XPS and ICP analysis

The atomic composition and chemical characteristics of the elements incorporated in the surface layer of modified $TiO_2$ were investigated by XPS (Fig. 5 and Table 2), and the bulk content of the doping elements in doped $TiO_2$ was measured by ICP-OES (Table 2).

As shown in Fig. 5(a), the Ti 2p region was composed of the Ti $2p_{3/2}$ peak and Ti $2p_{1/2}$ peak. The binding energies of the $2p_{3/2}$ peak and $2p_{1/2}$ peak were $458.5 \pm 0.1$ and $464.2 \pm 0.1$ eV and the area ratio of the two peaks was approximately 2.1 for all modified samples, which are in accordance with those of $Ti^{4+}$ [31,32]. Ti existing in the form of $Ti^{4+}$ without a low valence, such as $Ti^{3+}$, may be ascribed to the low content of the dopant [33] and to oxidization by adsorbed water [34] in the long hydrothermal synthesis process.

Table 2 shows that all samples contained carbon, ranging from 17.6% to 19.1%, as measured by XPS on the surface of the catalysts. This element was ascribed to the residual carbon from the precursor as the samples were prepared by the hydrothermal process at a relatively low temperature. The C 1s XPS spectra of LA10B50 are shown in Fig. 5(b) and were fitted to three peaks at binding energies of 284.8, 285.6, and 288.7 eV, suggesting adventitious elemental/aromatic carbon on the surface of the samples, C–OH bonds and C=O bonds of the surface-adsorbed carbonate species, respectively [11,31,35]. Therefore, all synthesized catalysts were covered with adventitious carbon species, which can alter surface layer features and extend the optical absorption of $TiO_2$ to visible light by photosensitivity [10,31].

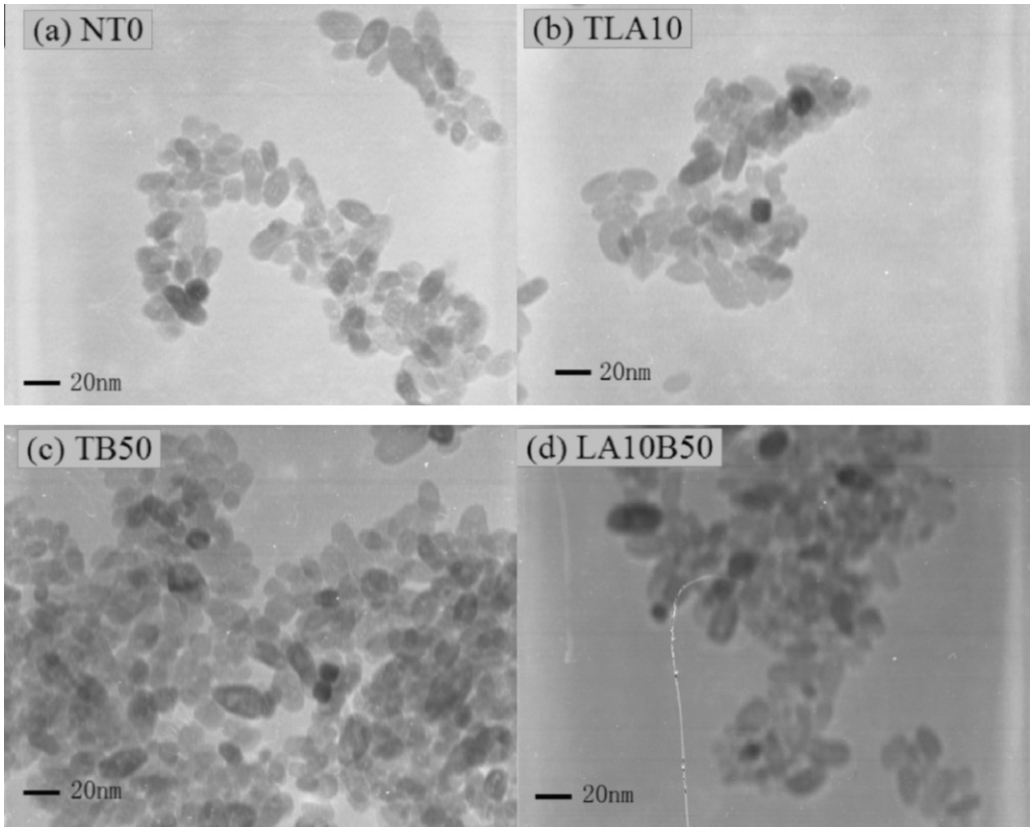


**Fig. 4.** TEM micrographs of (a) NT0, (b) TLA10, (c) TB50, and (d) LA10B50.

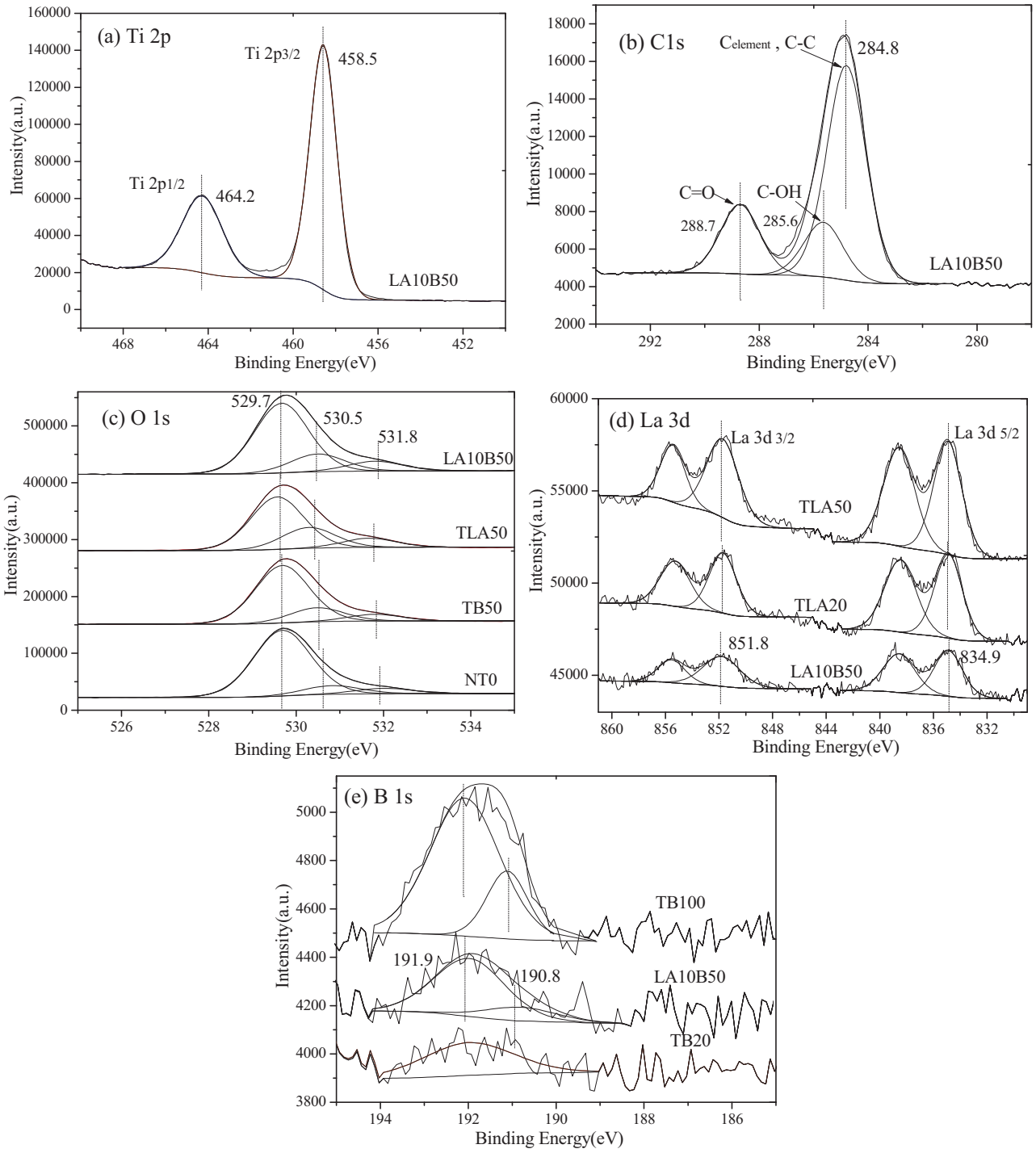


**Fig. 5.** High-resolution XPS spectra of the (a) Ti 2p region of LA10B50; (b) C 1s region of LA10B50; (c) O 1s region of NT0, TB50, TLA50, and LA10B50; (d) La 3d region of LA10B50, TLA20, and TLA50; (e) B 1s region of TB20, LA10B50, and TB100.

**Table 2**
Chemical surface La/Ti and B/Ti molar ratios by XPS, surface carbon atomic concentration by XPS and La/Ti and B/Ti molar ratios by ICP of the modified samples.

| | Sample | | | | | | | |
|---|---|---|---|---|---|---|---|---|
| | TLA10 | TLA20 | TLA50 | TB20 | TB50 | TB100 | LA10B20 | LA10B50 |
| $C_{(XPS)}$ (at.%) | 18.24 | 18.35 | 18.59 | 18.37 | 19.14 | 18.40 | 18.23 | 18.21 |
| $La/Ti_{(XPS)}$ | 0.0113 | 0.0233 | 0.0421 | – | – | – | 0.0129 | 0.0135 |
| $La/Ti_{(ICP)}$ | 0.0024 | 0.0051 | 0.0094 | – | – | – | 0.0022 | 0.0025 |
| $B/Ti_{(XPS)}$ | – | – | – | 0.0045 | 0.0128 | 0.0272 | 0.0047 | 0.0139 |
| $B/Ti_{(ICP)}$ | – | – | – | 0.0029 | 0.0079 | 0.0183 | 0.0028 | 0.0076 |

**Table 3**
Relative atomic percentage of $O_{(O-Ti)}$, $O_{(O-H)}$, and $O_{(O-C)}$ in non-doped and modified titanium catalysts.

| Sample | O $1s_{(Ti-O)}$ (at.%) | O $1s_{(O-H)}$ (at.%) | O $1s_{(C-O)}$ (at.%) |
|---|---|---|---|
| NT0 | 81.40 | 11.86 | 6.81 |
| TB20 | 75.88 | 15.49 | 8.63 |
| TB50 | 73.50 | 17.93 | 8.57 |
| TLA10 | 73.42 | 16.87 | 9.71 |
| TLA20 | 71.37 | 18.00 | 10.63 |
| TLA50 | 63.65 | 25.30 | 11.05 |
| LA10B50 | 71.71 | 18.22 | 10.07 |

The high-resolution O 1s spectra are asymmetric and can be fitted by three peaks including crystal lattice oxygen (Ti–O), hydroxyl group oxygen (H–O), and surface contaminant oxygen (C–O) with increasing binding energy (Fig. 5(c)). The corresponding atomic percentage composition of the three oxygen types is summarized in Table 3. The binding energies of Ti–O, O–H, and C–O were 529.7, 530.5, and 531.8 eV, respectively. Table 3 shows that the percentage of O atom in the Ti–O bond decreased, whereas the content of O atoms in the O–H and C–O bonds increased with La and B doping. The samples with La and B doping had larger specific surface areas, and their surface contained more carbohydrates which had oxygen atoms in the O–H or O–C bonds. The increase in surface hydroxyl content also results from element incorporation [11]. The hydroxyl groups are mainly ascribed to the chemisorbed water [36,37] and an increase in hydroxyl groups on the photocatalyst surface contributed to the improvement of photocatalytic activity [38,39].

In Fig. 5(d), the characteristic XPS splitting doublet peaks in the La 3d region appeared at 851.8 eV (La $3d_{3/2}$) and 834.9 eV (La $3d_{5/2}$) for all the La-doped catalysts. The fitted data are consistent with the standard spectrum of lanthanum oxide [29]. The apparent splitting of La bonding to oxygen is due to configuration effects in the final state of La [27], demonstrating that the La element trapped on the surface of the resulting catalysts exists in the form of $La_2O_3$.

Table 2 presents the La and B content of the surface and catalyst matrix measured from XPS and ICP-OES, respectively. The molar ratios of La/Ti in the bulk of the catalysts were 0.24%, 0.51%, 0.94%, 0.22%, and 0.25% for TLA10, TLA20, TLA50, LA10B20, and LA10B50, respectively. The corresponding surface molar ratios were 1.13%, 2.33%, 4.21%, 1.29%, and 1.35%, which are approximately 4.48–5.86 times larger than those inside the samples. These suggest that most of La was trapped on the surface of titanium during the hydrothermal doping process. The difference in radii between $La^{3+}$ (0.1016 nm) and $Ti^{4+}$ (0.068 nm) was the main reason why the $La^{3+}$ ion cannot easily enter the lattice of titanium to substitute the $Ti^{4+}$ ion by the hydrothermal process. The presence of doped La on the surface of the photocatalyst can cause a shallow capture trap, which benefits the photocatalytic reaction dominantly happening on the surface of the modified catalysts. The fast accepting of shallow capture current carriers from the interior of the nanoparticle by $La_2O_3$ leads to the efficient separation of photo-generated electron–hole pairs, which enhances the photocatalytic interface reaction [29,33]. Moreover, the low La ion content inside the $TiO_2$ prevents the trapping of the photo-generated carrier in the bulk of the catalyst and favors the diffusion process of the carriers [33].

The B 1s emission in Fig. 5(e) shows two peaks at the binding energy (BE) values of 191.9 and 190.8 eV in the TB50 and TB100 samples. The standard binding energies of B 1s in $B_2O_3$ or $H_3BO_3$ (193.0 eV, B–O bond) and in $TiB_2$ (187.5 eV, B–Ti bond) suggest that B is neither bonded by the B–Ti–B bond nor by the B–O bond within the as-prepared catalyst [12]. The radius of $B^{3+}$ (0.023 nm) was much smaller than that of $Ti^{4+}$ (0.064 nm), therefore, for $B^{3+}$ to replace the $Ti^{4+}$ site is difficult [40]. The low BE peak at 190.8 eV corresponds to B incorporated into the $TiO_2$ lattice through substitution of O sites to form B–Ti–O bonding [38,41]. The high BE peak at 191.9 eV is related to B ions in the interstitial of $TiO_2$ matrix to form Ti–O–B [12,42], which is the main form of B on the surface of the catalyst.

The quantitative analysis of doped B by XPS and ICP showed the diffusion feature of B in the catalysts. The XPS signal was very weak for B on the surface when the doping content was less than 2%, as in TB20 and LA10B20. When the molar ratios of B/Ti inside the catalysts measured by ICP were 0.29%, 0.79%, 1.83%, 0.28%, and 0.76% for TB20, TB50, TB100, LA10B20, and LA10B50, respectively, the corresponding molar ratios of B/Ti on the surface were 0.45%, 1.28%, 2.72%, 0.47%, and 1.39%, respectively, which are approximately 1.48–1.82 times larger than those inside the samples. This demonstrates that the B content increased from the interior to the surface of the catalyst.

## 4. Photocatalytic degradation under visible and solar light

The photocatalytic activities of the non-doped $TiO_2$, La–$TiO_2$, B–$TiO_2$, and La–B–$TiO_2$ catalysts were evaluated through PCP-Na (initial concentration of 20 ppm) degradation in aqueous solution under visible ($\lambda > 400$ nm) and solar light (20.6–37.9 mW/cm$^2$) for 2 h in Fig. 6(a) and (b). The initial adsorption of PCP-Na on nanopowders within 60 min in the dark is shown in Table 4. The decrease in PCP-Na concentration in the NT0 dispersed solution was inapparent and the adsorbed amount was higher on the surface of all the modified catalysts, especially for the La-doped and La–B co-doped catalyst, which were loaded with 23.3%–28.4% PCP-Na. The trend was ascribed to the increase in surface area, the enhancement of OH groups, and the presence of $La_2O_3$ coating on the surface of the catalysts. Blank experiments without photocatalysts were carried out to investigate the photodegradation of PCP-Na under visible and solar light, and the photolysis was 0.5% and 8% for 2 h visible and solar light illumination, respectively.

All the doped catalysts had a much higher activity than that of the non-doped photocatalyst under visible light, wherein the PCP-Na degradation was 15%. Solar light-induced photocatalysis was also investigated in Beijing in May. The relative concentrations of PCP-Na were fitted by the apparent first-order equation. The apparent reaction rate constants ($k_{Vis}$ and $k_{Solar}$) under visible light and solar light are listed in Table 4. A photodegradation of PCP-Na by P25 $TiO_2$ was also employed to clarify visible light response of the La and B modified $TiO_2$. From the rate constants, the visible photocatalytic activity of TLA20 and TB50 was highest among the La–$TiO_2$ and B–$TiO_2$ series, respectively. The photocatalytic degradation rates of TLA20 and TB50 were 4.66 and 4.48 times that on NT0, and the conversions of PCP-Na (for 120 min irradiation) were 88.4% and 90.1%, respectively. In comparison with the degradation rate constants utilizing La doped and B doped $TiO_2$ series, the commercial P25 $TiO_2$ exhibited very low photocatalytic activity in the degradation of PCP-Na with a rate constant of $0.054 \times 10^{-2}$ min$^{-1}$, which was approximately 50 times lower than that of TLA20 and TB50.

The reaction rate constant increased with the La/Ti molar ratio from 0% to 2%, and then decreased when the La/Ti molar ratio was 5% under visible light irradiation. However, the TLA20 sample was less active compared with TLA10 under solar light. The increased specific surface area and surface barriers leading to the efficient separation of electron hole pairs increased the photocatalytic activity of the La-modified $TiO_2$. However, when the coated $La_2O_3$ layer, which acts as a space charge region, is overloaded, the space charge region becomes very narrow. This occurs when surface barriers are enhanced, and the required depth of penetration of light into $TiO_2$ greatly exceeds the dimensions of the space charge layer [27]. Too much $La_2O_3$ trapped on the surface of $TiO_2$, such as in TLA50,

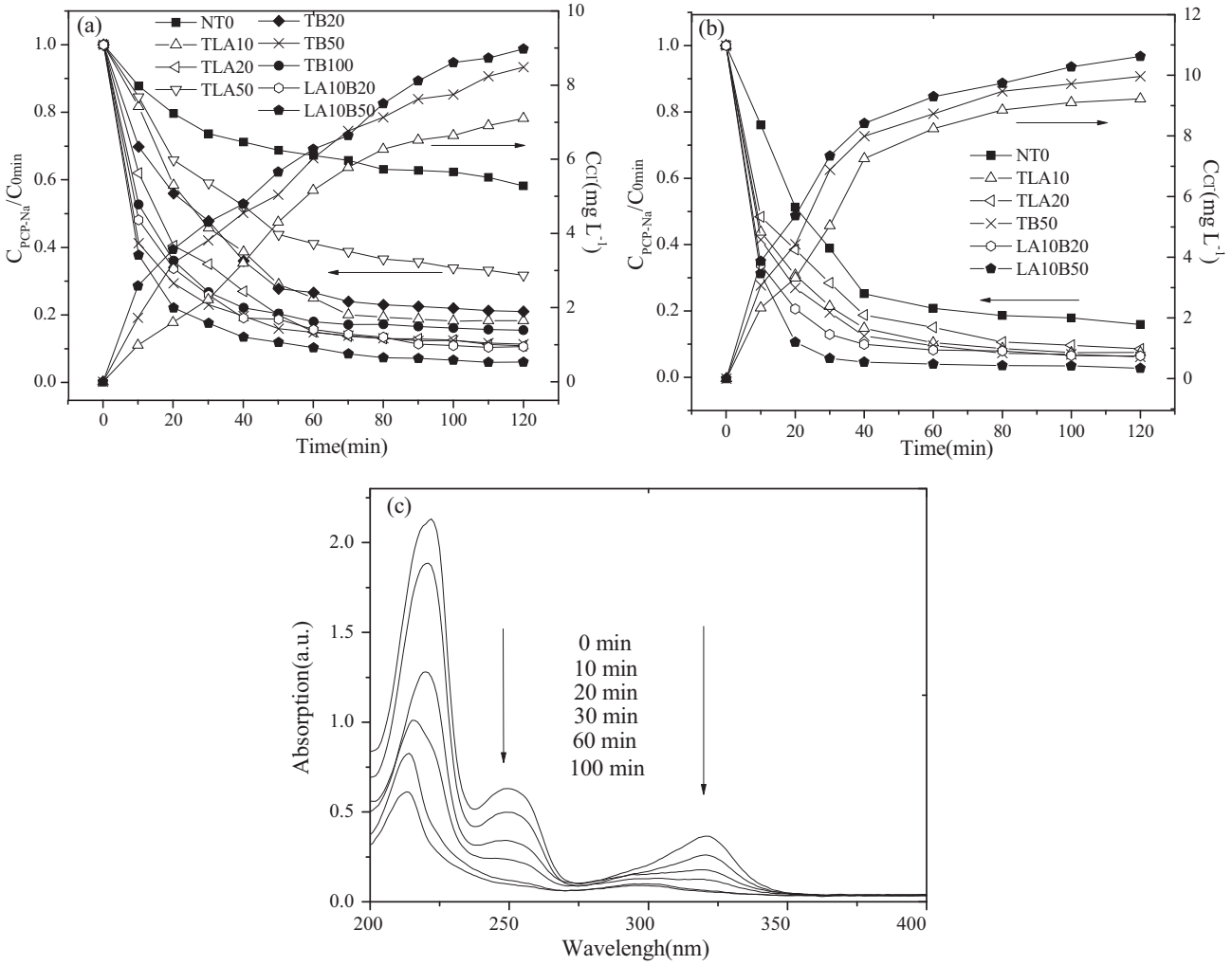


**Fig. 6.** Photodegradation of PCP-Na with modified $TiO_2$: (a) photocatalysis under visible light illumination, (b) photocatalysis under solar light irradiation, and (c) UV spectral changes in PCP-Na by LA10B50 under solar light irradiation.

can decrease the absorption of visible light because of its white color. In these cases, the easier recombination of the photo-induced electron–hole pairs and the weaker visible light absorption contribute to the worsening of photocatalytic activity. Thus, catalysts with 4.2% La coating and 2.3% La coating were overloaded under visible light and solar light, respectively.

The removal rate increased and then slightly decreased as the doping content of B increased from 1% to 10% in the following trend: TB50 > TB100 > TB20. The high activity of the B-doped $TiO_2$ series under visible and solar light was attributed to the midgap band arising from the substitutional B for oxygen atoms, interstitial B, and the formation of localized oxygen vacancies.

La–B co-doped $TiO_2$ nanoparticles exhibited a higher photocatalytic activity than La-doped and B-doped $TiO_2$ in removing PCP-Na from the aqueous solution under both visible and solar irradiation. The final concentrations of PCP-Na were approximately 1.2 and 0.54 ppm after 2 h of photocatalysis by LA10B50 under visible and solar light; the degradation efficiencies was 94.0% and 97.3%, respectively.

The dechlorination of PCP-Na is also illustrated in Fig. 6(a) and (b). The data for this reaction suggest that the activity of dechlorination was consistent with the photocatalytic degradation of PCP-Na for TLA10, TB50, and LA10B50. The chloride formation rates were slow compared with the degradation rate of PCP-Na, which indicates that the dechlorination is stepwise and also occurs in the degradation of the intermediates [43]. Photodecomposition of PCP-Na results from radicals (such as •OH and •OOH) attacking PCP-Na to replace chlorine atoms, which generates more hydroxyl functional groups such as semiquinone radicals [20,21]. The dechlorinated intermediates were subsequently oxidized to open up the aromatic ring. Finally, the substrate was mineralized to $CO_2$ and $H_2O$. The dechlorination efficiency under solar light was higher

**Table 4**
The adsorption of PCP-Na within 60 min in the dark and apparent first-order rate constant $k$ ($10^{-2}$ $min^{-1}$) for the photocatalytic degradation of PCP-Na under visible and solar light irradiation in the initial 60 min.

| | Catalyst | | | | | | | | |
|---|---|---|---|---|---|---|---|---|---|
| | NT0 | TB20 | TB50 | TB100 | TLA10 | TLA20 | TLA50 | LA10B20 | LA10B50 |
| $C_{0\,min}/C_0$ | 0.932 | 0.879 | 0.809 | 0.783 | 0.747 | 0.728 | 0.716 | 0.767 | 0.721 |
| $k_{Vis}$ | 0.640 | 2.690 | 2.864 | 2.236 | 2.371 | 2.985 | 1.504 | 2.865 | 3.439 |
| $k_{Solar}$ | 2.779 | – | 3.776 | – | 3.614 | 3.050 | – | 3.956 | 5.297 |

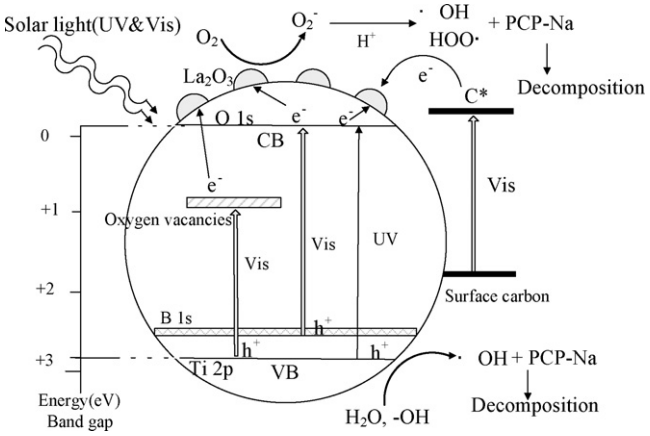


**Fig. 7.** Schematic illustration of the photocatalytic reaction by the La–B co-doped catalyst under solar light irradiation.

than that under visible light; the amount of released chloride ions was 2.21, 3.81, and 4.30 mg/L for TLA10, TB50, and LA10B50, respectively, after 30 min visible light irradiation. The corresponding results under solar light were 5.04, 6.88, and 7.34 mg/L.

The UV spectral variations during photocatalysis on LA10B50 are also presented in Fig. 6(c). The PCP-Na aqueous solution exhibited two major absorption peaks at 249 and 320 nm, which is attributed to the conjugated structure [23]. The absorption value at 249 and 320 nm decreased efficiently with the solar light-induced photocatalytic reaction.

The La–B co-doped $TiO_2$ presented the most activity toward PCP-Na under both visible light and solar light irradiation (Fig. 7), which can be attributed to the synergetic effects of La incorporation and B implantation. The La doping mainly responsible for the efficient separation of electron–hole pairs and B doping caused a red shift to the visible region. The other beneficial effects of the hydrothermal co-doping process included an increased amount of hydroxyl groups, a larger surface area, and the presence of carbon originating some visible-light responding.

## 5. Conclusions

La–B-modified $TiO_2$ series was fabricated by the sol–gel hydrothermal method to investigate the effect of La and B species on PCP-Na decomposition. The incorporation of La led to smaller anatase crystallite size and mosoporous framework, whereas B doping enlarged the grain size and mesoporous structure. When co-doped with La and B, a large surface area, a narrowed absorption band, and a small crystallite size were obtained. The narrowing of the absorption band mainly resulted from B doping, and not from La doping, due to $La_2O_3$ coating on the co-doped catalyst. XPS and ICP-OES showed that the entry of B into the lattice of $TiO_2$ was evidenced by the form of substitutional and interstitial B. The B content increased approximately 1.6 times in the interior compared with the surface of the modified catalyst. The presence of $La^{3+}$ was proven by XPS and ICP-OES as $La_2O_3$ on the surface of the nanoparticle. The photocatalytic degradation and dechlorination of PCP-Na over the La–B co-doped titania series revealed a high activity for the co-doped catalyst under both visible light and solar light. This was due to the efficient separation of photo-generated electron–hole pairs and visible light absorption, which resulted from the synergetic effects of the incorporation of La and B, respectively. The enhanced photocatalytic activity also resulted from hydroxyl groups and carbon species on the surface synthesized in the sol–gel hydrothermal process. The doped catalyst exhibited a higher activity under solar light illumination than under visible light irradiation. Therefore, the introduction of La and B into $TiO_2$ was proven to be effective in the photocatalytic decomposition of PCP-Na in aqueous medium and was favorable to photocatalysis under solar light.

## Acknowledgments

We gratefully acknowledge the financial support of the Natural Science Foundation of China (No. 40972152) and the key program of the National Hi-Tech R&D Project of China (No. 2009AA064001).

## References

[1] L. Lhomme, S. Brosillon, D. Wolbert, J. Photochem. Photobiol. A: Chem. 188 (2007) 34–42.
[2] K. Dai, T.Y. Peng, H. Chen, J. Liu, L. Zan, Environ. Sci. Technol. 43 (2009) 1540–1545.
[3] C. Lettmann, K. Hildenbrand, H. Kisch, W. Macyk, W.F. Maier, Appl. Catal. B: Environ. 32 (2001) 215–227.
[4] N. Venkatachalam, M. Palanichamy, B. Arabindoo, V. Murugesan, J. Mol. Catal. A: Chem. 266 (2007) 158–165.
[5] S. Rehman, R. Ullah, A.M. Butt, N.D. Gohar, J. Hazard. Mater. 170 (2009) 560–569.
[6] T. Sano, N. Negishi, K. Koike, K. Takeuchi, S. Matsuzawa, J. Mater. Chem. 14 (2004) 380–384.
[7] H. Irie, Y. Watanabe, K. Hashimoto, J. Phys. Chem. B 107 (2003) 5483–5486.
[8] T. Ohno, M. Akiyoshi, T. Umebayashi, K. Asai, T. Mitsui, M. Matsumura, Appl. Catal. A: Gen. 265 (2004) 115–121.
[9] T. Tachikawa, S. Tojo, K. Kawai, M. Endo, M. Fujitsuka, T. Ohno, K. Nishijima, Z. Miyamoto, T. Majima, J. Phys. Chem. B 108 (2004) 19299–19306.
[10] Y. Park, W. Kim, H. Park, T. Tachikawa, T. Majima, W. Choi, Appl. Catal. B: Environ. 91 (2009) 355–361.
[11] C. Jin, R.Y. Zheng, Y. Guo, J.L. Xie, Y.X. Zhu, Y.C. Xie, J. Mol. Catal. A: Chem. 313 (2009) 44–48.
[12] A. Zaleska, J.W. Sobczak, E. Grabowska, J. Hupka, Appl. Catal. B: Environ. 78 (2008) 92–100.
[13] A. Zaleska, E. Grabowska, J.W. Sobczak, M. Gazda, J. Hupka, Appl. Catal. B: Environ. 89 (2009) 469–475.
[14] N. Masahashi, M. Oku, Appl. Surf. Sci. 254 (2008) 7056–7060.
[15] H. Yamashita, M. Harada, J. Misaka, M. Takeuchi, K. Ikeue, M. Anpo, J. Photochem. Photobiol. A: Chem. 148 (2002) 257–261.
[16] T.Y. Han, C.F. Wu, C.T. Hsieh, J. Vac. Sci. Technol. B 25 (2007) 430–435.
[17] T.D. Nguyen-Phan, M.B. Song, E.J. Kim, E.W. Shin, Micropor. Mesopor. Mater. 119 (2009) 290–298.
[18] Y.N. Huo, J. Zhu, J.X. Li, G.S. Li, H.X. Li, J. Mol. Catal. A: Chem. 278 (2007) 237–243.
[19] S. Sanches, M.T.B. Crespo, V.J. Pereira, Water Res. 44 (2010) 1809–1818.
[20] M. Fukushima, K. Tatsumi, Environ. Sci. Technol. 35 (2001) 1771–1778.
[21] Q. Lan, F.B. Li, C.X. Sun, C.S. Liu, X.Z. Li, J. Hazard. Mater. 174 (2010) 64–70.
[22] K. Morimoto, K. Tatsumi, Chemosphere 34 (1997) 1277–1283.
[23] X.F. Chang, J. Huang, Q.Y. Tan, M. Wang, G.B. Ji, S.B. Deng, G. Yu, Catal. Commun. 10 (2009) 1957–1961.
[24] S. Song, J.J. Tu, Z.Q. He, F.Y. Hong, W.P. Liu, J.M. Chen, Appl. Catal. A: Gen. 378 (2010) 169–174.
[25] G.D. Yang, Z. Jiang, H.H. Shi, M.O. Jones, T.C. Xiao, P.P. Edwards, Z.F. Yan, Appl. Catal. B: Environ. 96 (2010) 458–465.
[26] T. Puangpetch, T. Sreethawong, S. Yoshikawa, S. Chavadej, J. Mol. Catal. A: Chem. 287 (2008) 70–79.
[27] Z.Q. He, X. Xu, S. Song, L. Xie, J.J. Tu, J.M. Chen, B. Yan, J. Phys. Chem. C 112 (2008) 16431–16437.
[28] R. Khan, S.W. Kim, T.J. Kim, C.M. Nam, Mater. Chem. Phys. 112 (2008) 167–172.
[29] G.X. Cao, Y.G. Li, Q.H. Zhang, H.Z. Wang, J. Hazard. Mater. 178 (2010) 440–449.
[30] B.M. Reddy, I. Ganesh, A. Khan, J. Mol. Catal. A: Chem. 223 (2004) 295–304.
[31] K. Chen, J.Y. Li, J. Li, Y.M. Zhang, W.X. Wang, Colloids Surf. A: Physicochem. Eng. Aspects 360 (2010) 47–56.
[32] F.M. John, F.S. William, E.S. Peter, Handbook of X-ray Photoelectron Spectroscopy, Perkin-Elmer, Minnesota, 2002.
[33] D.P. Xu, L.J. Feng, A.L. Lei, J. Colloid Interface Sci. 329 (2009) 395–403.
[34] S. Yuan, Q.R. Sheng, J.L. Zhang, H. Yamashita, D.N. He, Micropor. Mesopor. Mater. 110 (2008) 501–507.
[35] Y.W. Wang, Y. Huang, W.K. Ho, L.Z. Zhang, Z.G. Zou, S.C. Lee, J. Hazard. Mater. 169 (2009) 77–87.
[36] K.L. Lv, H.S. Zuo, J. Sun, K.J. Deng, S.C. Liu, X.F. Li, D.Y. Wang, J. Hazard. Mater. 161 (2009) 396–401.
[37] J.G. Yu, G.H. Wang, B. Cheng, M.H. Zhou, Appl. Catal. B: Environ. 69 (2007) 171–180.
[38] J.J. Xu, Y.H. Ao, M.D. Chen, D.G. Fu, J. Alloys Compd. 484 (2009) 73–79.
[39] P. Du, A. Bueno-Lopez, M. Verbaas, A.R. Almeida, M. Makkee, J.A. Moulijn, G. Mul, J. Catal. 260 (2008) 75–80.
[40] D. Chen, D. Yang, Q. Wang, Z.Y. Jiang, Ind. Eng. Chem. Res. 45 (2006) 4110–4116.
[41] X. Zhang, Q.Q. Liu, Mater. Lett. 62 (2008) 2589–2592.
[42] Y. Huang, W.K. Ho, Z.H. Ai, X.A. Song, L.Z. Zhang, S.C. Lee, Appl. Catal. B: Environ. 89 (2009) 398–405.
[43] T.C. Wang, N. Lu, J. Li, Y. Wu, Environ. Sci. Technol. 44 (2010) 3105–3110.